THE JOURNAL OF PHYSICAL CHEMISTRY C

Article

pubs.acs.org/JPCC

One-Step, Cooperative Deposition of Au−Ni Alloy Nanoparticles on a Si Substrate: "Catalytic" Growth Mechanism in an Aqueous Medium

Liyan Zhao, Nina Heinig, and K. T. Leung*

WATLab and Department of Chemistry, University of Waterloo, Waterloo, Ontario, Canada N2L 3G1

Supporting Information

ABSTRACT: Gold−nickel alloy nanoparticles are prepared on a H-terminated Si(100) substrate by a simple, one-step cooperative electrochemical deposition process at room temperature. The spherical alloy nanoparticles, with an average diameter of 6−12 nm, are obtained by amperometry at −0.8 V (with respect to a Ag/AgCl reference electrode) for 2−10 s in an aqueous solution of 0.05 mM $AuCl_3$, 5 mM $NiCl_2$, and 100 mM $NaClO_4$. Depth-profiling X-ray photoelectron spectroscopy reveals interesting evolution in Au 4f or/and Ni 2p binding energy shifts with respect to sputtering depth, which supports the formation of a Au−Ni alloy during the codeposition via a new "catalytic" growth mechanism. In particular, Au nanocrystallites that are deposited first onto the substrate act as a catalyst to initiate the subsequent Ni deposition. Codeposition of Au and Ni then occurs simultaneously, and the presence of Au and Ni nanodeposits further promotes the growth of each other, producing alloy nanoparticles. The glancing-incidence X-ray diffraction pattern of the new Au−Ni nanoparticles exhibits a small shift to larger 2θ, corresponding to smaller lattice parameters, than pristine Au nanoparticles, confirming the alloy formation. The Au−Ni alloy formation by coelectrochemical deposition promises potential applications in designing new catalysts.

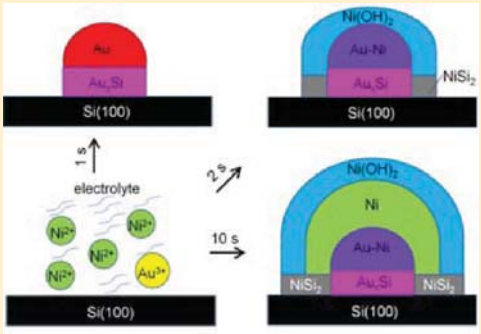

1. INTRODUCTION

Metallic alloy nanoparticles (NPs) are known to exhibit special structural, mechanical, magnetic, and catalytic properties not found in single-metallic NPs.[1−3] They have attracted a lot of attention due to their potential industrial applications.[4] For example, PdAu alloy NPs supported on TiO_2 demonstrated improved activity and selectivity for benzyl alcohol oxidation compared to supported pure Au and pure Pd catalysts.[5] In the case of Au and Ni, the binary phase diagram of Au and Ni exhibits a large miscibility gap, indicating that Au−Ni alloy can only be formed at elevated temperature and not at room temperature.[6] To date, only a "surface" Au−Ni alloy was observed in the topmost atomic layer of the Ni(110)[7] and Ni(111)[8] surfaces upon Au thermal evaporation by using scanning tunneling microscopy and was also predicted to be energetically favorable by calculations based on the effective-medium theory.[7−9] Boerma et al. also studied the arrangement of Au atoms segregated to the Ni(110) surface by heating and found the presence of a surface Au−Ni alloy only on the outermost atomic layer by using low-energy ion scattering and low-energy electron diffraction.[10] Au−Ni alloy NPs have also been prepared by simultaneous reduction of metal salt precursors with appropriate reducing agents.[11,12] Furthermore, there have been a few studies on relatively thick Au−Ni alloy films with a thickness of a few micrometers obtained by electrodeposition/electroplating.[13−15] Only two studies on producing bulk Au−Ni alloy NPs by electrochemistry have been reported, and both employed electrochemical deposition (ECD) of two metal ions in a solution containing the appropriate electrolytes to produce Au−Ni alloy NPs. In particular, Lu et al. prepared Au−Ni alloy NPs onto an amorphous carbon electrode by ECD in an aqueous solution containing 1.0 mM $HAuCl_4$, 1.0 mM $NiSO_4$, and 50 mM $CsClO_4$.[16] Their transmission electron microscopy (TEM) data showed the presence of multiply twinned nanocrystallites in these Au−Ni alloy NPs (22−30 nm in size). The radii of the diffraction rings of these Au−Ni alloy NPs were reported to be larger than that of pure Au particles, and the deduced smaller lattice spacings were used as the only evidence for alloying. Surprisingly, individual Au or Ni components on these NPs were ruled out by Lu et al., despite the relatively higher deposition rate of Au expected from their working electrolyte consisting of equal concentrations of $AuCl_4^+$ and Ni^{2+}. Dolati et al. also reported the formation of a Au−Ni alloy film with thickness of 100 nm on a copper wire by ECD at a current density of 3 mA cm^{-2} for 3 s in cyanide-citrate electrolytes.[17] However, the corresponding TEM analysis of a representative deposit only showed an electron diffraction pattern consistent with fcc Au that exhibited a preferred (111) orientation with a significant (200) reflection. The Au−Ni alloy so obtained revealed a uniform gold texture with a single-phase fcc structure containing a few rectangular nuclei of nickel, which suggests

Received: March 11, 2012
Revised: May 7, 2012
Published: May 23, 2012

that their electrodeposits consisted of individual Au and Ni grains instead of alloy as claimed. These previous studies therefore highlight the challenges in synthesizing Au−Ni alloy nanostructured materials and the need for spectroscopic composition analysis to fully characterize the intriguing growth evolution of these alloy nanomaterials.

Among the various methods used to prepare metallic NPs on a substrate, ECD is an attractive synthetic technique because not only is it a simple, inexpensive, rapid, and easily scalable method but also the particle shape, size, density, and distribution of the electrodeposits can be easily controlled by manipulating the deposition potential, current, and other parameters. In the present work, we report the formation of Au−Ni alloy NPs by single-step, co-ECD for the first time onto a H-terminated Si(100) substrate. Since a H-terminated Si(100) substrate provides an atomically flat surface, it is chosen to avoid the complexity introduced by the substrate in our study of the formation mechanism of the Au−Ni alloy NPs. By comparing to results obtained with two-step sequential ECD, these experiments provide strong evidence for a new catalytic growth mechanism, with the initially formed Au nuclei acting as catalysts to promote the subsequent Au−Ni alloy growth.

2. EXPERIMENTAL DETAILS

All the ECD experiments are performed in a three-electrode cell with a CH Instruments 660A potentio/galvanostat electrochemical workstation. The working electrodes are single-side-polished, p-type Si(100) chips (15 × 2.5 mm^2, 0.4 mm thick) with a resistivity of 1.0−1.5 mΩ·cm, which have been hydrogen terminated by a standard procedure. Si(100) chips are cleaned by using the RCA method, etched in an aqueous HF (2%) solution to remove the native oxide layer, and rinsed thoroughly with Millipore water.[18] A standard Ag/AgCl reference electrode and a platinum-wire counter electrode are used in all the ECD experiments. In a deoxygenated aqueous solution containing specified concentrations of $AuCl_3$ and/or $NiCl_2$, along with 100 mM $NaClO_4$ serving as the supporting electrolyte, the deposition is conducted on the H-terminated Si substrate by amperometry at a constant potential (vs Ag/AgCl). After the deposition, the sample is thoroughly rinsed with Millipore water and dried in N_2, before further analysis of the resulting electrodeposits.

The surface morphology and elemental composition of the resulting electrodeposits are characterized by scanning electron microscopy (SEM) and energy-dispersive X-ray analysis (EDX), respectively, using a LEO 1530 field-emission SEM equipped with an EDAX Pegasus system. The corresponding chemical-state composition is analyzed by X-ray photoelectron spectroscopy (XPS) as a function of argon ion sputtering time in a Thermo-VG Scientific ESCALab 250 Microprobe equipped with a monochromatic Al Kα X-ray source (1486.6 eV), at a typical energy resolution of 0.4−0.5 eV full-width at half-maximum. The binding energy scale is calibrated to that of the Si $2p_{3/2}$ photopeak of bulk Si (99.3 eV).[19] Argon ion sputtering is performed over a rastered area of 4 × 4 mm^2 of the sample at an ion beam energy of 3 keV and a typical sample current density of 108 nA mm^{-2}. The structural characterization of the nanodeposits is determined by glancing-incidence X-ray diffraction (GIXRD) at an incidence angle of 0.6°, using a PANalytical MRD X'pert Pro diffractometer with the Cu Kα anode operating at 45 kV and 35 mA.

3. RESULTS AND DISCUSSION

3.1. Au−Ni Alloy Formation As Functions of Deposition Potential, Deposition Time, and Ni^{2+}-to-Au^{3+} Concentration Ratio. For the aqueous electrolyte solution containing 5 mM $AuCl_3$, 5 mM $NiCl_2$, and 100 mM $NaClO_4$, we set the potential used for co-ECD to −1.2 V (vs Ag/AgCl) because this potential is found, in separate experiments, to readily facilitate the deposition of metallic Ni NPs onto the H-terminated Si substrate in an electrolyte solution containing 5 mM $NiCl_2$ (and 100 mM $NaClO_4$). However, even for a relatively long deposition time of 100 s, EDX analysis shows only the Au signal with no detectable Ni signal from the sample. The electrodeposits are found to be dominated by metallic Au, when the initial Ni^{2+}-to-Au^{3+} concentration ratio or $[Ni^{2+}]/[Au^{3+}]$ is set to 1. We then reduce the $AuCl_3$ concentration to 0.05 mM while keeping the other electrolyte components at 5 mM $NiCl_2$ (i.e., with $[Ni^{2+}]/[Au^{3+}]$ = 100) and 100 mM $NaClO_4$. By adjusting the concentration of Au^{3+} ions in the solution, we in effect bring the individual reversible potentials closer to each other, thereby enabling codeposition of both Au and Ni. With $[Ni^{2+}]/[Au^{3+}]$ set to 100, we perform co-ECD for 10 s at a series of potentials, including −0.6, −0.8, −1.0, and −1.2 V (vs Ag/AgCl), and find that −0.8 V is the least negative working potential that provides nanodeposits with detectable Au and Ni EDX signals. We have therefore chosen −0.8 V (vs Ag/AgCl) as the deposition potential for all subsequent experiments.

With $[Ni^{2+}]/[Au^{3+}]$ set to 100, we investigate the growth evolution of the nanodeposits by performing co-ECD at −0.8 V (vs Ag/AgCl) for several deposition times. For a deposition time of 1 s, spherical NPs with an average diameter of 6 nm are observed by using SEM (Figure 1a), while the corresponding

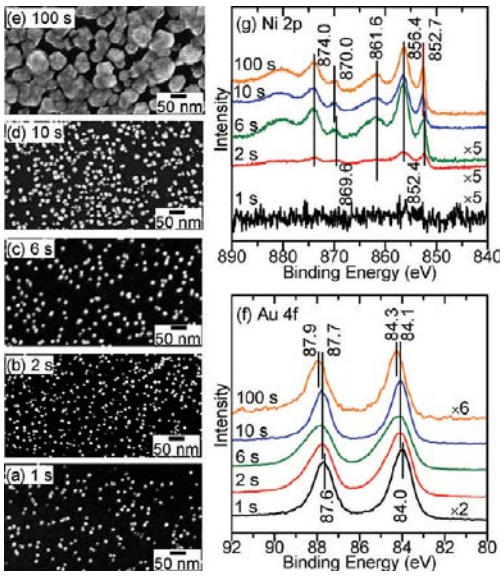

Figure 1. SEM images of Au or Au−Ni alloy nanoparticles obtained by electrodeposition in a solution of 0.05 mM $AuCl_3$, 5 mM $NiCl_2$, and 100 mM $NaClO_4$ at −0.8 V (vs Ag/AgCl) for (a) 1 s, (b) 2 s, (c) 6 s, (d) 10 s, and (e) 100 s and corresponding XPS spectra of (f) Au 4f and (g) Ni 2p regions of the as-prepared samples. To compensate for the smaller amounts of nanodeposits obtained by the 1, 2, and 6 s deposition, a larger pass energy of 40 eV was used, compared to that (20 eV) employed for collecting spectra of the samples obtained by the 10 and 100 s deposition.

dx.doi.org/10.1021/jp302336k | J. Phys. Chem. C 2012, 116, 12322−12329

EDX analysis reveals no detectable Au or Ni. For a 2 s deposition, more nanodeposits with the same average size of 6 nm and an increased surface density are obtained (Figure 1b). Increasing the deposition time to 6 s evidently produces NPs with a larger average size of 10 nm (Figure 1c). For a 10 s deposition, very densely dispersed, spherical NPs with an average diameter of 12 nm are obtained (Figure 1d), and the corresponding EDX analysis indicates that both Ni and Au are present on the sample, with a Ni-to-Au atomic ratio of 5.6. When the deposition time is increased to 100 s, agglomeration of NPs into a film is clearly observed (Figure 1e), with the corresponding EDX analysis giving a Ni-to-Au ratio of 19.2.

The corresponding Au 4f and Ni 2p XPS spectra of the nanodeposits obtained with different deposition times are also shown in Figure 1f and 1g, respectively. For the 1 s co-ECD, we can clearly verify the presence of a well-resolved Au $4f_{7/2}$ ($4f_{5/2}$) feature at 84.0 eV (87.6 eV) corresponding to metallic Au,[20] while no detectable Ni 2p signal is obtained. For 2 and 6 s co-ECD, the Au $4f_{7/2}$ ($4f_{5/2}$) features at 84.1 eV (87.7 eV) and Ni $2p_{3/2}$ ($2p_{1/2}$) features at 852.4 eV (869.6 eV) give binding energy shifts of +0.1 and −0.3 eV from the respective metallic positions of Au (84.0 eV) and Ni (852.7 eV).[21,22] The binding energy shifts in opposite direction clearly support the assignment of these features to Au−Ni alloy.[23] It should be noted that for Au NPs smaller than 1−2 nm the Au 4f binding energy increases with decreasing Au NP size.[24] However, given that the smallest metallic Au NPs (6 nm) obtained in the present work (i.e., by 1 s co-ECD) have the same binding energy as metallic Au, there is no quantum size effect for the NPs of the present size regime. The observed binding energy shifts are therefore not due to quantum size effect. For 10 and 100 s co-ECD, the Au $4f_{7/2}$ ($4f_{5/2}$) peak located at 84.1 eV (87.7 eV) and 84.3 eV (87.9 eV), respectively, can also be attributed to the surface Au−Ni alloy. The minor binding energy shifts from metallic Au for the 10 and 100 s co-ECD samples are 0.1 and 0.3 eV, respectively, which is also indicative of the formation of bimetallic alloy.[25] The difference observed in the binding energy shift is due to the different Au−Ni alloy composition in the two samples. The corresponding Ni $2p_{3/2}$ ($2p_{1/2}$) peak at 852.7 eV (870.0 eV) for both 10 and 100 s co-ECD samples is found to be in excellent accord with metallic Ni. The lack of a discernible Ni $2p_{3/2}$ alloy peak is likely due to the presence of an additional metallic Ni shell covering the Au−Ni alloy core. The thicker metallic Ni shell for the 100 s co-ECD sample also substantially reduces the observed Au 4f signal from the Au−Ni alloy core (Figure 1f; note the change in the intensity scale). Except for the 1s co-ECD sample, all other samples also exhibit another Ni $2p_{3/2}$ ($2p_{1/2}$) feature at 856.4 eV (874.0 eV), which can be attributed to surface $Ni(OH)_2$.[26] The broad Ni $2p_{3/2}$ ($2p_{1/2}$) peak found at 861.6 eV (880.0 eV) corresponds to the shakeup Ni 2p excitation of $Ni(OH)_2$.[26]

Figure 2 compares the corresponding GIXRD patterns of the Au−Ni alloy NPs obtained by co-ECD at −0.8 V (vs Ag/AgCl) for 10 s and for 100 s. For the 10 s co-ECD sample, we observe, in addition to the Si(311) diffraction features at 50−60°, a set of diffraction peaks slightly shifted from the reference pattern of the fcc phase of metallic Au (JCPDS 65-2870), which confirms the predominant presence of Au−Ni alloy. For the 100 s co-ECD sample, we observe an additional set of diffraction peaks corresponding to the fcc phase of metallic Ni (JCPDS 65-2865). This is quite evident from the exceptionally intense feature at 44.49° found for the 100 s co-ECD sample, which can be attributed mainly to the Ni(111) feature in spite of the close-lying Au(200) feature, and from the strong features at 76.38° and 92.93°, attributed to Ni(220) and Ni(311), respectively. Furthermore, the small shifts to a larger 2θ found for the Au−Ni alloy features are larger (with respect to Au fcc) for the 100 s co-ECD sample than the 10 s co-ECD sample. It should be noted that according to Bragg's law the (111) plane should exhibit the biggest shift when the lattice parameters change. The Au−Ni alloy (111) feature is shifted by 0.056° and 0.137° for the 10 s and 100 s co-ECD samples, respectively. Using the 2θ value of the Au−Ni alloy (111) feature and the Bragg equation, we calculate the corresponding lattice constants of the Au−Ni alloy NPs for the 10 s (4.0735 Å) and 100 s co-ECD samples (4.0646 Å). From these calculated lattice constants and the chart of lattice spacing vs composition given by Person,[27] we deduce the composition of the Au−Ni alloy NPs to be $Au_{99}Ni_1$ for the 10 s co-ECD and $Au_{97}Ni_3$ for the 100 s co-ECD. While all the deposited Au atoms predominantly exist in the Au−Ni alloy form, the majority of the deposited Ni atoms (not involved in the Au−Ni alloy) is present in the form of a fcc metallic Ni shell on top of the Au−Ni alloy core or as a $Ni(OH)_2$ skin on the Ni shell. The considerably larger Ni-to-Au atomic ratios obtained from our EDX measurement for the 100 s co-ECD sample (19.2) relative to that for the 10 s sample (5.6) therefore suggest the presence of a sizable Ni shell in the 100 s co-ECD sample.

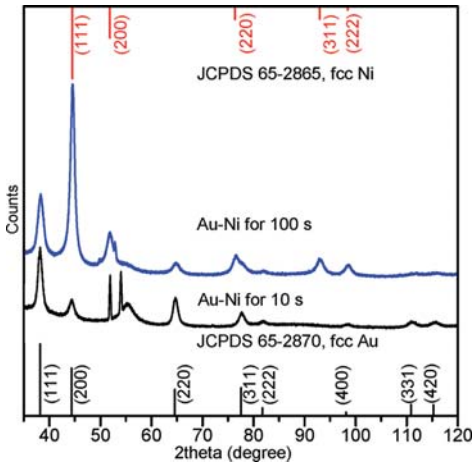

Figure 2. Comparison of the reference JCPDS 65-2870 for fcc Au (bottom bar chart) and reference JCPDS 65-2865 for fcc Ni (top bar chart) with GIXRD patterns of Au−Ni alloy nanoparticles obtained by coelectrodeposition in a solution of 0.05 mM $AuCl_3$, 5 mM $NiCl_2$, and 100 mM $NaClO_4$ at −0.8 V (vs Ag/AgCl) for 10 s and 100 s.

To investigate the effect of the relative concentrations between Au^{3+} and Ni^{2+} on the initial stage of alloy formation, we compare the nanodeposits obtained by co-ECD with $[Ni^{2+}]/[Au^{3+}]$ = 1000 and 10 with that by co-ECD with $[Ni^{2+}]/[Au^{3+}]$ = 100. By performing ECD with $[Ni^{2+}]/[Au^{3+}]$ increased from 100 (Figure 1a, Figure 3b) to 1000, i.e., using an aqueous electrolyte solution containing 50 mM $NiCl_2$, 0.05 mM $AuCl_3$, and 100 mM $NaClO_4$, at −0.8 V (vs Ag/AgCl) for 1 s, we obtain homogeneous, uniformly distributed nanodeposits with an average size of 8 nm (Figure 3a). The corresponding XPS analysis reveals a Au $4f_{7/2}$ peak located at 84.6 eV (Figure 3g), i.e., 0.6 eV higher than the metallic Au binding energy, which confirms the presence of Au−Ni alloy in the NPs. Compared to the deposition with $[Ni^{2+}]/[Au^{3+}]$ = 100, the much higher Ni^{2+} concentration enables the Ni

dx.doi.org/10.1021/jp302336k | J. Phys. Chem. C 2012, 116, 12322−12329

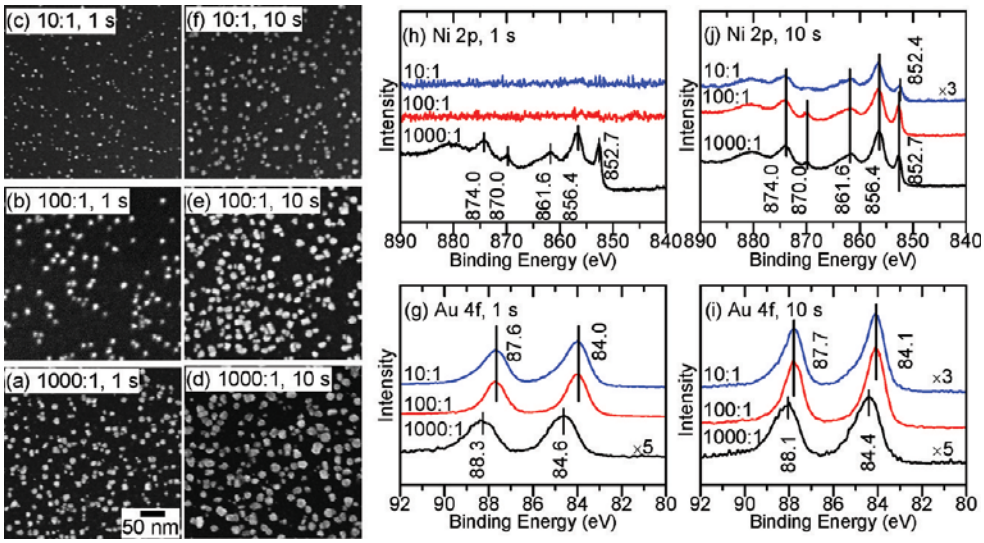

Figure 3. SEM images (a–f) and XPS spectra of (g, i) Au 4f and (h, j) Ni 2p regions for Au or Au–Ni alloy nanoparticles obtained by electrodeposition at −0.8 V (vs Ag/AgCl) and for (a, b, c) 1 s and (d, e, f) 10 s in a solution of (a, d) 50 mM $NiCl_2$, 0.05 mM $AuCl_3$, and 100 mM $NaClO_4$ (corresponding to $[Ni^{2+}]/[Au^{3+}] = 1000$); (b, e) 5 mM $NiCl_2$, 0.05 mM $AuCl_3$, and 100 mM $NaClO_4$ (corresponding to $[Ni^{2+}]/[Au^{3+}] = 100$); and (c, f) 0.5 mM $NiCl_2$, 0.05 mM $AuCl_3$, and 100 mM $NaClO_4$ (corresponding to $[Ni^{2+}]/[Au^{3+}] = 10$). To compensate for the smaller amounts of nanodeposits obtained at 1 s, all the corresponding XPS spectra are collected with a larger pass energy of 40 eV.

deposition to occur at a shorter time after the Au–Ni alloy formation. For 10 s deposition time, Au–Ni alloy nanoparticles with an average diameter of 20 nm are obtained (Figure 3d), and the corresponding Au $4f_{7/2}$ peak located at 84.4 eV (Figure 3i) is found to be 0.4 eV higher than the metallic Au binding energy, which again confirms the presence of Au–Ni alloy in the NPs. In both cases, the Ni $2p_{3/2}$ located at 852.7 eV is assigned to metallic Ni (Figures 3h, 3j), and the presence of this strong metallic Ni feature likely overwhelms the presence of any weak Ni 2p feature attributable to Au–Ni alloy. On the other hand, by conducting ECD with $[Ni^{2+}]/[Au^{3+}]$ reduced to 10, with a solution of 0.5 mM $NiCl_2$, 0.05 mM $AuCl_3$, and 100 mM $NaClO_4$, at −0.8 V (vs Ag/AgCl) for 1 s, only metallic Au NPs with an average diameter of 2 nm are obtained, just like the case of $[Ni^{2+}]/[Au^{3+}] = 100$. For the 10 s deposition time, Au–Ni alloy NPs with an average diameter of 5 nm are obtained, and the corresponding Ni $2p_{3/2}$ peak located at 852.4 eV for the nanodeposits (Figure 3j) is found to be 0.3 eV lower than the metallic Ni binding energy, which also confirms the formation of Au–Ni alloy in the NPs. As with the case of $[Ni^{2+}]/[Au^{3+}] = 100$, the presence of the strong Au $4f_{7/2}$ ($4f_{5/2}$) metallic feature at 84.1 eV (87.7 eV) is attributable to Au–Ni alloy. For different Ni^{2+}-to-Au^{3+} concentration ratios with the $AuCl_3$ concentration fixed at 0.05 mM, the binding energy shift of at least one of Au 4f or Ni 2p is observed when both Au and Ni XPS features are detectable (as in the 10 s co-ECD sample). The presence of this binding energy shift provides strong evidence for the alloy formation. In separate experiments, we have also done electrodeposition for the three different Ni^{2+}-to-Au^{3+} concentration ratios with the $AuCl_3$ concentration increased to 0.5 mM (Supporting Information, Figure S1). The higher relative concentration of the Au^{3+} ion in the solution with $[Ni^{2+}]/[Au^{3+}] = 10$ (5 mM $NiCl_2$, 0.5 mM $AuCl_3$, and 100 mM $NaClO_4$), compared to that in the solution with $[Ni^{2+}]/[Au^{3+}] = 100$ (5 mM $NiCl_2$, 0.05 mM $AuCl_3$, and 100 mM $NaClO_4$, Figure 3), leads to the early formation of a greater number of Au nuclei, which then promote the subsequent Ni electrodeposition to form Au–Ni alloy. These experiments show that a minimal critical relative Au concentration is needed to initiate the Au–Ni alloy formation at a short deposition time of 1 s for a solution with a particular Ni^{2+} ion concentration.

3.2. Depth-Profiling XPS Study of Au–Ni Alloy Nanoparticles and Proposed Growth Model. To investigate the nature of Au–Ni alloy nanoparticles obtained by co-ECD, we perform depth-profiling XPS of the Au 4f (Figure 4a) and Ni 2p regions (Figure 4b) to determine the relative chemical-state composition of the NPs deposited with $[Ni^{2+}]/[Au^{3+}] = 100$ at −0.8 V (vs Ag/AgCl) for 10 s (Figure 1d). For the as-prepared sample, the Au $4f_{7/2}$ ($4f_{5/2}$) peak located at 84.1 eV (87.7 eV) has been assigned to surface Au–Ni alloy, while the Ni $2p_{3/2}$ ($2p_{1/2}$) peaks at 852.7 eV (870.0 eV) and at 856.4 eV (874.0 eV) correspond to metallic Ni and surface $Ni(OH)_2$, respectively. Upon sputtering for 5 s, the Au $4f_{7/2}$ peak becomes broader and can be resolved into two components: a Au–Ni alloy feature at 84.2 eV (i.e., 0.2 eV higher than the metallic Au feature) and a new Au silicide feature (Au_xSi) at 85.2 eV (Figure 4a).[28] The formation of the Au silicide feature for Au NPs electrodeposited onto the H–Si substrate has been discussed in detail in our earlier work.[28] Continued sputtering to 245 s evidently reduces the Au–Ni alloy feature, while a steady increase in the relative intensity of the Au silicide feature is observed. The Au–Ni alloy feature is totally removed after 485 s of sputtering. In contrast, no Ni 2p component with a discernible binding energy shift relative to that of metallic Ni is observed in the corresponding Ni 2p spectrum after 5 s of sputtering (Figure 4b). This is because the presence of the strong metallic Ni feature likely overwhelms the weak Ni 2p feature attributable to Au–Ni alloy. Upon sputtering for 35 s, the surface $Ni(OH)_2$ feature has evidently been totally removed, while the metallic Ni $2p_{3/2}$ feature remains unchanged at 852.7 eV for sputtering up to 65 s. The removal of the $Ni(OH)_2$ feature also exposes the presence of the corresponding Ni $2p_{3/2}$ shakeup peak at 858.5 eV due to metallic Ni. Further sputtering to 245 s appears to cause the sharp Ni $2p_{3/2}$ feature to shift to 853.7 eV, which remains at the same binding

dx.doi.org/10.1021/jp302336k | J. Phys. Chem. C 2012, 116, 12322–12329

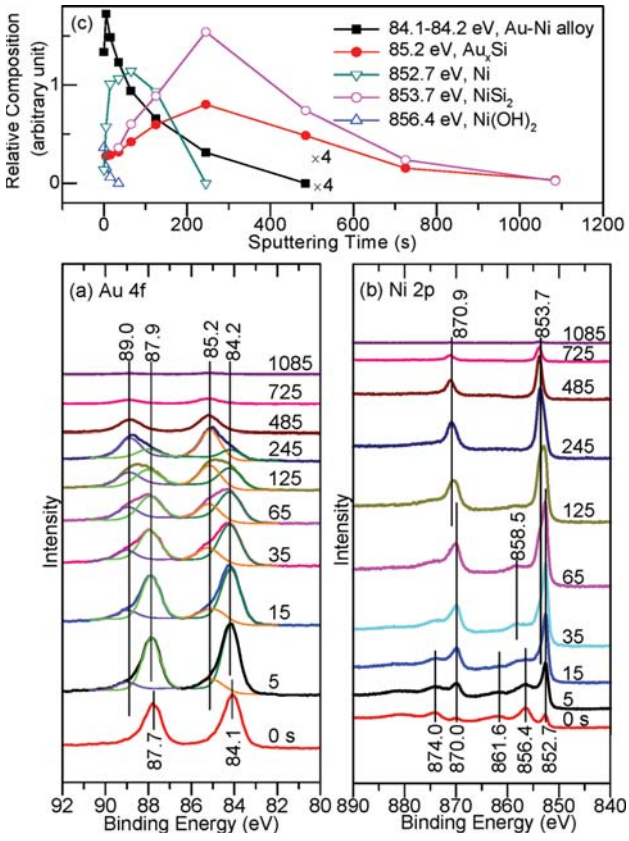

Figure 4. XPS spectra of (a) Au 4f and (b) Ni 2p regions, obtained as a function of sputtering time, and (c) depth profiles of Au $4f_{7/2}$ features at 84.1−84.2 eV (alloy) and 85.2 eV (Au silicide) and of Ni $2p_{3/2}$ features at 852.7 eV (metallic Ni), 853.7 eV (Ni disilicide), and 856.4 eV [$Ni(OH)_2$] for Au−Ni alloy nanoparticles electrodeposited on H:Si in a solution of 0.05 mM $AuCl_3$, 5 mM $NiCl_2$, and 100 mM $NaClO_4$ at −0.8 V (vs Ag/AgCl) for 10 s.

energy position but becomes weaker upon further sputtering to 725 s. In accord with the literature,[29] this new Ni $2p_{3/2}$ feature at 853.7 eV corresponds to Ni disilicide ($NiSi_2$). Both of the remaining Au silicide and Ni disilicide features are completely removed upon further sputtering to 1085 s.

From the depth-profiling XPS spectra, we obtain the corresponding depth profiles (Figure 4c) for the respective Au $4f_{7/2}$ and Ni $2p_{3/2}$ features for the 10 s co-ECD sample by appropriate peak fitting of the observed XPS features. Starting backward from the long to short sputtering time, i.e., from the Si substrate to the top of electrodeposits, we observe broad profiles of the Au silicide and Ni disilicide with maxima at 245 s sputtering time. The Au−Ni alloy feature first emerges at 485 s sputtering time and peaks at 5 s, while the metallic Ni feature appears at 245 s with a narrow profile with maximum at 65 s. Depth-profiling XPS spectra are also performed on the 100 s co-ECD sample. The evolution of the Au $4f_{7/2}$ and Ni $2p_{3/2}$ spectra as a function of sputtering time for the 100 s co-ECD sample (Supporting Information, Figure S2) is found to be very similar to that of the 10 s co-ECD sample (Figure 4). However, a discernible change in the binding energy of the Au $4f_{7/2}$ feature (Supporting Information, Figure S2) from 84.3 eV (corresponding to surface Au−Ni alloy) before sputtering to 84.4 eV (corresponding to bulk Au−Ni alloy) upon sputtering is observed. The binding energy of the main Au $4f_{7/2}$ peak (84.4 eV) for the "bulk" Au−Ni alloy for the 100 s co-ECD sample is also discernibly larger than that for the 10 s co-ECD sample (84.2 eV). This should be due to changes in the composition of the Au−Ni alloy and the strengthening of bonding between Au and Ni for the co-ECD sample with a longer deposition time. The amount of Au−Ni alloy and metallic Ni was also larger for the 100 s co-ECD sample.

To investigate the notion of cooperative catalytic growth in the co-ECD process, we compare the corresponding ECD experiments obtained with just one metal electrolyte solution. For the aqueous solution containing just 5 mM $NiCl_2$ and 100

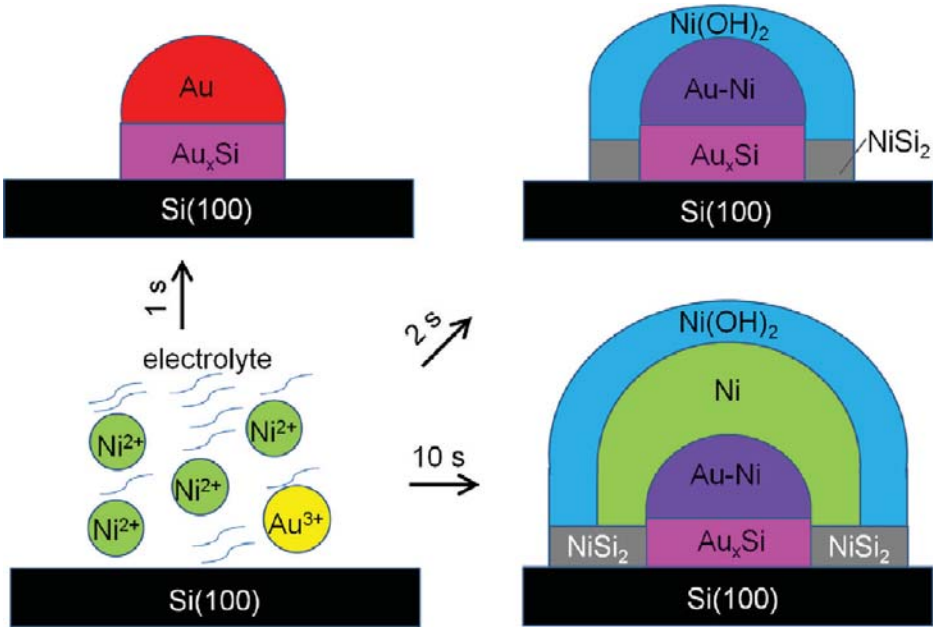

Figure 5. Growth models of Au−Ni alloy nanoparticles by codeposition from a solution of 0.05 mM $AuCl_3$, 5 mM $NiCl_2$, and 100 mM $NaClO_4$ at −0.8 V (vs Ag/AgCl) for short and longer deposition times.

dx.doi.org/10.1021/jp302336k | J. Phys. Chem. C 2012, 116, 12322−12329

mM $NaClO_4$ (i.e., without the $AuCl_3$ electrolyte), no metallic Ni is observed for ECD at −0.8 V (vs Ag/AgCl) for 10 s. On the other hand, for the aqueous solution containing 0.05 mM $AuCl_3$ and 100 mM $NaClO_4$ (i.e., without the $NiCl_2$ electrolyte), spherical Au NPs with an average diameter of 5 nm are obtained at −0.8 V (vs Ag/AgCl) for 10 s. However, the atomic ratio of Au-to-Si is found to be 0.06 from their respective XPS features, which is significantly lower than that obtained from co-ECD under the same conditions (0.21). For the aqueous solution containing 5 mM $NiCl_2$ and 100 mM $NaClO_4$ but with 0.05 mM $AuCl_3$ added, co-ECD at −0.8 V for 10 s produces homogeneous Au−Ni NPs (shown in Figure 1d). Co-ECD therefore appears to enhance and promote NP growth of both Au and Ni.

Since the standard reduction potential of Au/Au^{3+} (1.498 V) is more positive than that of Ni/Ni^{2+} (−0.257 V),[30] the electrodeposition rate of Au is much higher than that of the Ni metal. It is therefore not surprising that at the beginning of the co-ECD Au nanocrystallites would be deposited first, and they then work as catalysts to promote the Ni deposition. Once the initial Ni deposition occurs, two parallel reactions involving Au^{3+} and Ni^{2+} could then proceed simultaneously, with Au depositing at a faster rate than Ni. Any deposited Ni atoms would quickly come in contact with (the more readily deposited) Au atoms to form Au−Ni alloy NPs. When no more Au^{3+} ions are available in the diffusion region (i.e., after all the Au^{3+} ions have reacted), subsequent deposition of the excess metallic Ni would occur on the top of the Au−Ni alloy NPs and eventually be covered by surface $Ni(OH)_2$. It should be noted while the addition of Au ions to an electrolytic solution containing Ni ions could change the solution equilibrium and shift the redox potential of Ni/Ni^{2+}, leading to codeposition of Au and Ni, this is not observed in the present case because co-ECD in the solution with $[Ni^{2+}]/[Au^{3+}] = 10$ for 1 s does not produce any metallic Ni. This therefore indicates that even for the highest relative concentration of Au employed in the present study the Au concentration is not sufficiently high to cause a shift in the redox potential.

Figure 5 shows a schematic model for the growth evolution of the Au−Ni alloy NP. For a very short deposition of 1 s, XPS analysis of the as-deposited NPs reveals only a Au 4f signal without any Ni 2p signal (Figure 1), which indicates that initial electrodeposition only leads to the formation of metallic Au NPs, with part of the deposited Au atoms reacting with Si to form Au silicide at the interface as discussed in our previous work.[28] For the deposition with a slightly longer deposition time of 2 s, the initially deposited Au nanocrystallites work as catalysts to facilitate the codeposition of Au and Ni. For co-ECD with a smaller deposition time than 10 s, i.e., 2 and 6 s, no metallic Ni is detected on top of the alloy, and the resulting NPs only consist of Au silicide at the interface and Au−Ni alloy core but with a thin $Ni(OH)_2$ skin. The Au NPs obtained by 1 s co-ECD is therefore the actual electrode interface for the initial formation of the Au−Ni alloy. (The spacing between the Au NPs and the size of the Au NPs affects whether the diffusion layers are isolated or merged. The effect of the Au nuclei on the diffusion layer in the subsequent electrodeposition is complicated and will require further studies.) Extending the deposition to 10 s produces a thick metallic Ni layer on the as-formed Au−Ni alloy core. For both samples obtained with co-ECD for 10 and 100 s, all the Au^{3+} ions from the 0.05 mM $AuCl_3$ component of the electrolyte are first consumed to form the Au−Ni alloy, except for the interface between the alloy NPs and the Si substrate where Au silicide formation is observed. In both cases, metallic Ni is predominantly electrodeposited on the top of the Au−Ni alloy core. Our XPS results also support the formation of a $Ni(OH)_2$ skin on the top of the Ni shell component of the NPs (with the Au−Ni alloy core) with Au silicide and Ni disilicide at the Si interface. While the as-prepared Au−Ni alloy NPs have an exterior consisting of either a $Ni(OH)_2$ skin or a $Ni(OH)_2$ skin plus a Ni shell, we do not expect the exterior to hinder the catalytic properties of the core. This is supported by a recent report that the core−shell structure of Co_xO_y-Pd has provided a significantly higher reforming reactivity due to the important role of the Co_xO_y core in the partial oxidation and CO activation.[31]

3.3. One-Step co-ECD vs Two-Step Sequential ECD.

We also compare the single-step co-ECD growth with a two-step sequential ECD process. In this sequential process, we perform ECD first in a solution of 0.05 mM $AuCl_3$ and 100 mM $NaClO_4$ at −0.8 V (vs Ag/AgCl) for 10 s (Step A), to be followed by ECD in a solution of 5 mM $NiCl_2$ and 100 mM $NaClO_4$ at −0.8 V (vs Ag/AgCl) for 10 s (Step B). It is not useful to perform the sequential deposition in the reverse order because performing Step B first will not result in any Ni deposition, while continuing with Step A will produce only spherical Au NPs, both of which have been demonstrated above. The SEM images show that the spherical Au NPs with an average diameter of 5 nm obtained in Step A (Figure 6a)

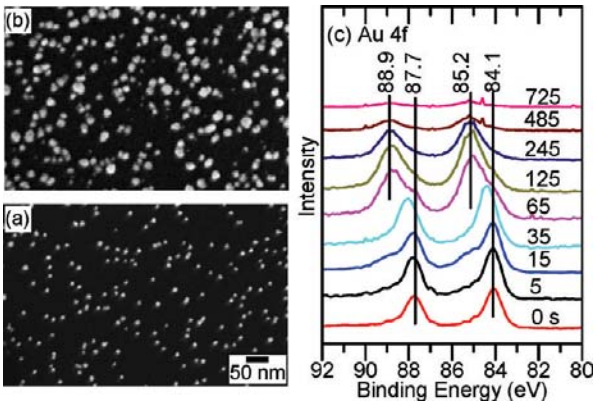

Figure 6. SEM image of nanoparticles produced by sequential electrodeposition after (a) Step A, at −0.8 V (vs Ag/AgCl) for 10 s in a solution of 0.05 mM $AuCl_3$ and 100 mM $NaClO_4$, and (b) Step B, at −0.8 V (vs Ag/AgCl) for 10 s in a solution of 5 mM $NiCl_2$ and 100 mM $NaClO_4$, and (c) the corresponding Au 4f XPS depth-profiling spectra of the resulting Au−Ni alloy nanoparticles.

become larger in size (~20 nm) due to Ni growth on the top of Au NPs in Step B (Figure 6b). The corresponding XPS data (Figure 6c) indicate the presence of a Au $4f_{7/2}$ peak at 84.1 eV, characteristic of the Au−Ni alloy formation, and depth profiles similar to those found for co-ECD at −0.8 V for 10 s (Figure 1d). Furthermore, we could increase the size of the Au NPs considerably to 21 nm by performing Step A at a more negative potential of −1.2 V for a longer time of 1800 s (Figure 7a) and investigate the size effect of the Au NPs on the subsequent Ni deposition in Step B (i.e., ECD as before at −0.8 V for 10 s). The resulting Ni-coated Au NPs are also found to be larger in size (Figure 7b). Interestingly, the Au $4f_{7/2}$ feature stays at the same binding energy position (84.0 eV) as that of pure Au NPs

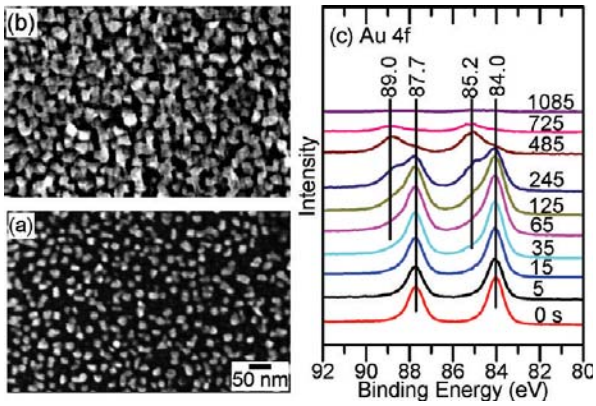

Figure 7. SEM image of nanoparticles produced by sequential electrodeposition after (a) Step A, at −1.2 V (vs Ag/AgCl) for 1800 s in a solution of 0.05 mM $AuCl_3$ and 100 mM $NaClO_4$, and (b) Step B, at −0.8 V (vs Ag/AgCl) for 10 s in a solution of 5 mM $NiCl_2$ and 100 mM $NaClO_4$, and (c) the corresponding Au 4f XPS depth-profiling spectra of the resulting nanoparticles.

in the corresponding depth-profiling XPS data (Figure 7c). The absence of any Au $4f_{7/2}$ feature at a higher binding energy indicates no Au−Ni alloy formation. This result suggests that the deposited Ni only reacts with the smaller Au NPs (up to a maximum size of ∼5 nm) to effect the Au−Ni alloy formation and that the formation of Au−Ni alloy is not due to a template-mediated growth mechanism. It should be noted that we have also collected Ni 2p spectra as a function of sputtering time and observed spectral evolution similar to Figure 4b. As in Figure 4b, the intense Ni 2p feature from the metallic Ni shell (not shown) tends to overwhelm that from the Au−Ni alloy core and is therefore not an effective indicator for the formation of Au−Ni alloy.

4. CONCLUSION

Spherical nanoparticles of an average size of 12 nm, each with a Au-Ni alloy core and a Ni shell, are prepared on a H-terminated Si(100) substrate by co-ECD at −0.8 V (vs Ag/AgCl) for 10 s in a solution of 0.05 mM $AuCl_3$, 5 mM $NiCl_2$, and 100 mM $NaClO_4$. Depth-profiling XPS and GIXRD data both confirm the formation of the Au−Ni alloy core and the presence of a Ni shell. For the as-prepared samples obtained by 2 s and 6 s co-ECD, the Au $4f_{7/2}$ and Ni $2p_{3/2}$ give binding energy shifts of +0.1 and −0.3 eV from the respective metallic positions. In addition to the observed binding energy shifts, the opposite direction of these binding energy shifts further supports the formation of Au−Ni alloy. During the co-ECD, the deposition of Au occurs first, and the resulting Au nanodeposits act as "catalysts" to initiate and promote the subsequent growth of Ni, forming the Au−Ni alloy core. This is then followed by simultaneous deposition of both Au and Ni (at different rates), which mutually accelerates the growth of each other. Upon consumption of Au^{3+} ions in the diffusion region, the remaining Ni deposition produces the Ni shell. In this proposed cooperative "catalytic" growth mechanism, the initial electro-deposited Au nuclei work like an "electrocatalyst" to facilitate metallic Ni deposition at a relatively low potential, even though it is eventually being consumed in its reaction with the deposited Ni atoms to form the Au−Ni alloy core. Of particular interest is that this "electrocatalyst" property only occurs for Au NPs smaller than ∼5 nm, which suggests the remarkable reactivity of a Au nanometer particle. The Au−Ni alloy core can also promote the growth of the two metals and may also be considered as an electrocatalyst. The present application of co-ECD can be generalized to other bimetallic systems including the Au−Cu and Au−Pd (and other multimetallic) systems.[32] The alloy composition can be fine-tuned by carefully manipulating the deposition potential, deposition time, and the $[Ni^{2+}]/[Au^{3+}]$ concentration ratio. The resulting Au−Ni alloy nanoparticles so optimized could potentially be used as model catalysts in the steam-forming process of hydrocarbons[33] or as good support for surface-enhanced Raman spectroscopy.[34]

■ ASSOCIATED CONTENT

Supporting Information

Au 4f and Ni 2p XPS spectra for nanoparticles obtained by electrodeposition at −0.8 V (vs Ag/AgCl) for 1 s and 10 s in electrolyte solutions involving three different Ni^{2+}-to-Au^{3+} concentration ratios with the $AuCl_3$ concentration fixed at 0.5 mM. Au 4f and Ni 2p depth profiling XPS spectra and depth profiles of alloy, metallic, and silicide components of Au−Ni alloy nanoparticles electrodeposited in a solution of 0.05 mM $AuCl_3$, 5 mM $NiCl_2$, and 100 mM $NaClO_4$ at −0.8 V (vs Ag/AgCl) for 100 s. This material is available free of charge via the Internet at http://pubs.acs.org.

■ AUTHOR INFORMATION

Corresponding Author

*E-mail: tong@uwaterloo.ca.

Notes

The authors declare no competing financial interest.

■ ACKNOWLEDGMENTS

This work was supported by the Natural Sciences and Engineering Research Council of Canada.

■ REFERENCES

(1) Sinfelt, J. H. *Bimetallic Catalysts. Discoveries, Concepts, and Applications*; Wiley: New York, 1983.
(2) Elkalkouli, R.; Grosbras, M.; Dinhut, J. F. *Nanostruct. Mater.* **1995**, *5*, 733−743.
(3) Kumbhar, A.; Spinu, L.; Agnoli, F.; Wang, K. Y.; Zhou, W. L.; O'Connor, C. J. *IEEE Trans. Magn.* **2001**, *37*, 2216−2218.
(4) Caruta, B. M. *Nanomaterials: New Research*; Nova Science: New York, 2005.
(5) Enache, D. I.; Edwards, J. K.; Landon, P.; Solsona-Espriu, B.; Carley, A. F.; Herzing, A. A.; Watanabe, M.; Kiely, C. J.; Knight, D. W.; Hutchings, G. J. *Science* **2006**, *311*, 362−365.
(6) Massalski, T. B. *Binary Alloy Phase Diagrams*; American Society for Metals: Metals Park, OH, 1986.
(7) Nielsen, L. P.; Besenbacher, F.; Stensgaard, I.; Lægsgaard, E.; Engdahl, C.; Stoltze, P.; Jacobsen, K. W.; Nørskov, J. K. *Phys. Rev. Lett.* **1993**, *71*, 754−757.
(8) Jacobsen, J.; Nielsen, L. P.; Besenbacher, F.; Stensgaard, I.; Lægsgaard, E.; Rasmussen, T.; Jacobsen, K. W.; Nørskov, J. K. *Phys. Rev. Lett.* **1995**, *75*, 489−492.
(9) Ruban, A. V.; Skriver, H. L.; Nørskov, J. K. *Phys. Rev. B* **1999**, *59*, 15990−16000.
(10) Boerma, D. O.; Dorenbos, G.; Wheatley, G. H.; Buck, T. M. *Surf. Sci.* **1994**, *307−309*, 674−679.
(11) Vasquez, Y.; Luo, Z. P.; Schaak, R. E. *J. Am. Chem. Soc.* **2008**, *130*, 11866−11867.
(12) Zhou, S. H.; Yin, H. F.; Schwartz, V.; Wu, Z. L.; Mullins, D.; Eichhorn, B.; Overbury, S. H.; Dai, S. *ChemPhysChem* **2008**, *9*, 2475−2479.

(13) He, A.; Liu, Q.; Ivey, D. G. *Plat. Surf. Finish.* **2009**, *96*, 22−29.
(14) Rouya, E.; Stafford, G. R.; Bertocci, U.; Mallett, J. J.; Schad, R.; Begley, M. R.; Kelly, R. G.; Reed, M. L.; Zangari, G. *J. Electrochem. Soc.* **2010**, *157*, D396−D405.
(15) Inoue, T.; Sato, K.; Yokoshima, T.; Sugiyama, A.; Okinaka, Y.; Osaka, T. *J. Electrochem. Soc.* **2011**, *158*, D403−D407.
(16) Lu, D. L.; Domen, K.; Tanaka, K. I. *Langmuir* **2002**, *18*, 3226−3232.
(17) Dolati, A.; Ghorbani, M.; Ahmadi, M. R. *J. Electroanal. Chem.* **2005**, *577*, 1−8.
(18) Kern, W. *Handbook of Semiconductor Wafer Cleaning Technology*; Noyes: Park Ridge, 1993.
(19) Sacher, E.; McIntyre, N. S. *Phys. Rev. B* **1986**, *33*, 2845−2846.
(20) Jiang, P.; Porsgaard, S.; Borondics, F.; KÖber, M.; Caballero, A.; Bluhm, H.; Besenbacher, F.; Salmeron, M. *J. Am. Chem. Soc.* **2010**, *132*, 2858−2859.
(21) Tam, P. L.; Nyborg, L. *Surf. Coating. Tech.* **2009**, *203*, 2886−2890.
(22) Moulder, J. F.; Stickle, W. F.; Sobol, P. E.; Bomben, K. D. *Handbook of X-ray Photoelectron Spectroscopy*, 2nd ed.; Chastain, J., Ed.; Perkin-Elmer Corp.: Eden-Prairie, 1992.
(23) Rousset, J. L.; Cadete Santos Aires, F. J.; Sekhar, B. R.; Mélinon, P.; Preve, B.; Pellarin, M. *J. Phys. Chem. B* **2000**, *104*, 5430−5435.
(24) Astruc, D. *Nanoparticles and Catalysis*; Wiley-VCH: Weinheim, 2008.
(25) Kim, M. J.; Na, H. J.; Lee, K. C.; Yoo, E. A.; Lee, M. *J. Mater. Chem.* **2003**, *13*, 1789−1792.
(26) Armitage, D. A.; Grant, D. M. *Mater. Sci. Eng., A* **2003**, *349*, 89−97.
(27) Person, W. B. *A Handbook of Lattice Spacings and Structures of Metals and Alloys*; Pergamon: London, 1958.
(28) Zhao, L. Y.; Siu, A. C. -L.; Petrus, J. A.; He, Z. H.; Leung, K. T. *J. Am. Chem. Soc.* **2007**, *129*, 5730−5734.
(29) Ok, Y. W.; Seong, T. Y.; Choi, C. J.; Tu, K. N. *J. Mater. Sci: Mater. Electron.* **2006**, *17*, 979−985.
(30) Lide, D. R. *CRC Handbook of Chemistry and Physics*, 84th ed.; CRC Press: Boca Raton, 2003.
(31) Kwak, B. S.; Kim, J.; Kang, M. *Int. J. Hydrogen Energy* **2010**, *35*, 11829−11843.
(32) Zhao, L. Y.; Leung, K. T. 2012, to be submitted.
(33) Chin, Y.-H.; King, D. L.; Roh, H.-S.; Wang, Y.; Heald, S. M. *J. Catal.* **2006**, *244*, 153−162.
(34) Bao, F.; Li, J. F.; Ren, B.; Yao, J. L.; Gu, R. A.; Tian, Z. Q. *J. Phys. Chem. C* **2008**, *112*, 345−350.